Ghaderzadeh, Sadegh; Ladygin, Vladimir; Ghorbani-Asl, Mahdi; Hlawacek, Gregor; Schleberger, Marika; Krasheninnikov, Arkady V.

Freestanding and Supported MoS_2 Monolayers under Cluster Irradiation : Insights from Molecular Dynamics Simulations

Published in:
ACS applied materials & interfaces

DOI:
10.1021/acsami.0c09255

Published: 19/08/2020

Document Version
Publisher's PDF, also known as Version of record

ACS APPLIED MATERIALS & INTERFACES

www.acsami.org

Research Article

Freestanding and Supported MoS_2 Monolayers under Cluster Irradiation: Insights from Molecular Dynamics Simulations

Sadegh Ghaderzadeh,* Vladimir Ladygin, Mahdi Ghorbani-Asl, Gregor Hlawacek, Marika Schleberger, and Arkady V. Krasheninnikov*

Cite This: *ACS Appl. Mater. Interfaces* 2020, 12, 37454–37463

Read Online

ACCESS | Metrics & More | Article Recommendations

ABSTRACT: Two-dimensional (2D) materials with nanometer-size holes are promising systems for DNA sequencing, water purification, and molecule selection/separation. However, controllable creation of holes with uniform sizes and shapes is still a challenge, especially when the 2D material consists of several atomic layers as, e.g., MoS_2, the archetypical transition metal dichalcogenide. We use analytical potential molecular dynamics simulations to study the response of 2D MoS_2 to cluster irradiation. We model both freestanding and supported sheets and assess the amount of damage created in MoS_2 by the impacts of noble gas clusters in a wide range of cluster energies and incident angles. We show that cluster irradiation can be used to produce uniform holes in 2D MoS_2 with the diameter being dependent on cluster size and energy. Energetic clusters can also be used to displace sulfur atoms preferentially from either top or bottom layers of S atoms in MoS_2 and also clean the surface of MoS_2 sheets from adsorbents. Our results for MoS_2, which should be relevant to other 2D transition metal dichalcogenides, suggest new routes toward cluster beam engineering of devices based on 2D inorganic materials.

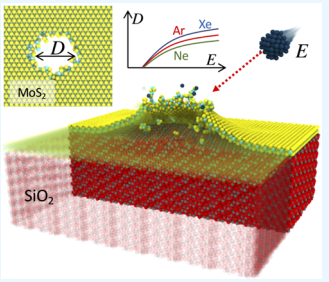

KEYWORDS: *two-dimensional materials, MoS_2, cluster irradiation, pore formation, sputtering yield, atomistic simulations*

INTRODUCTION

After nearly 2 decades since the first exfoliation of individual sheets from graphite and inorganic compounds with a layered structure,[1] two-dimensional (2D) materials continue to surprise us, as more and more potential applications of these systems are revealed.[2] In particular, creating nanoscale pores in these atomically thin impervious membranes and using the holey material for DNA sequencing, water purification, separation of chemical species, etc. has been suggested.[3−8] This should allow us to develop a new generation of DNA and complex protein sequencers with unprecedented speed, precision, and low cost, which may revolutionize genomic medicine.[5−8] As for particle selection/separation, having nanopores of the right sizes in 2D materials allows only the desired ions/molecules to pass through the pores and block unwanted particles.[3,4]

It is intuitively clear that the precise control over the sizes of the pores is the key to the successful use of 2D materials in these applications. Various techniques can be employed to perforate graphene and inorganic 2D materials such as h-BN or transition metal dichalcogenides (TMDs). Among them, lithographic patterning using block copolymers,[9] positive e-beam resist,[10] and other mask materials have been used to create periodic arrays of holes in graphene, the so-called nanomesh, which is interesting in the context of tuning the electronic properties of the system. However, these techniques provided holes with diameters of tens of nanometers, which may be too large for, e.g., molecule separation. Preparation of holey graphene via catalytic oxidation[11] has also been reported, but controlling the uniformity of hole sizes and shapes is a challenge.

Another group of methods to produce holes in 2D systems relies on applying beams of energetic particles, ions and electrons, and changing the atomic structure of the target material by ballistically displacing the atoms.[12−14] In particular, electron irradiation in the transmission electron microscope (TEM) has been demonstrated to produce holes with diameters of few nanometers in graphene,[15−18] h-BN,[19,20] and TMDs.[21−23] Although the electron beam in a scanning TEM can nowadays be focused into a sub-angstrom area, potentially providing unprecedented control over the sizes and shapes of the holes, this technique cannot be scaled up to produce enough material even at the tens-of-micrometer scale.

Ion irradiation has successfully been used to create defects in various 2D materials[14,24−26] or directly implant dopants.[27,28] However, impacts of individual ions with most easily accessible low charge states and moderate energies produce predom-

Received: May 20, 2020
Accepted: July 28, 2020
Published: July 28, 2020

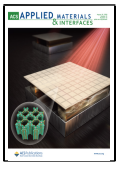

https://dx.doi.org/10.1021/acsami.0c09255
ACS Appl. Mater. Interfaces 2020, 12, 37454–37463

inantly single vacancies and small vacancy clusters[14,26] and not holes with diameters of few nanometers. Besides, irradiation in this case gives rise to the formation of defects with different sizes. Focused ion beams, especially in the He-ion microscope (HIM), have been demonstrated to be suitable for patterning various 2D materials,[24,29−33] and creating pores, but the main drawback of this approach is the collateral damage to the material close to the holes due to the spread of the beam and, in the case of supported materials, due to the ions backscattered from the substrate.[34] Swift heavy ions can produce larger holes in semiconducting 2D materials[35] and even in semimetallic graphene either supported[36] or free-standing,[37] once the electronic stopping exceeds a certain threshold value,[37] but the availability of such facilities is limited.

Using highly charged but relatively slow ions is another approach to perforate 2D materials. In this case, the charge state of the incident ion is the parameter that controls the potential energy stored in the ion and allows additional energy to be deposited into the target,[38] so that ions with higher charge states produce larger pores. Highly charged ions have been successfully used to create pores with controllable diameters of a few nanometers in 2D MoS_2.[39] For low charge states, the size distribution of these pores turned out to be rather small (full width at half-maximum (FWHM) = 0.75 nm), whereas for higher charge states, it quickly increased to larger values (FWHM = 1.75 nm). The pore shapes were generally round, but more irregular shapes with jagged edges were also frequently found.

A more uniform distribution of the hole sizes may be achieved, however, using cluster irradiation, as, contrary to single-ion impacts, the outcome of collision weakly depends on the impact point, as clusters are normally larger than the primitive cell size of the material. Atomistic simulations of cluster impacts onto graphene[40−42] and polycrystalline boron-nitride nanosheets[43] indicate that the size of the hole correlates well with the size of the cluster and indeed pore diameters are more uniform. These simulations have been carried out for truly single-layer structures, and it is not obvious how this approach works for 2D materials, which, e.g., TMDs, consist of several atomic layers. Besides, mostly freestanding 2D materials have been studied, while the substrate can completely govern defect production[44] and annealing[45] in supported 2D materials.

In this article, using analytical potential molecular dynamics (MD) simulations, we study the response of MoS_2 sheets, both freestanding and supported by a SiO_2 substrate, to cluster irradiation. MoS_2, which consists of three atomic layers, is the archetypical TMD material. Besides, holey MoS_2 is expected to be efficient for gas separation[46] and water desalination.[47] We consider impacts of clusters of various noble gas atoms (Ne, Ar, Kr, and Xe) in a wide range of energies. Note that by using noble gas clusters, chemical reactions between the cluster and target atoms are avoided. We model both normal and grazing trajectories, as the latter can be used to displace sulfur atoms predominantly from one side of the sheet, and, followed by the deposition of other chemical elements, e.g., Se, manufacture the so-called Janus structures,[48] tuning thus the electronic properties of the material.[31] Off-normal cluster irradiation can also be employed for cleaning the surface of MoS_2 from ubiquitous hydrocarbons or removing small flakes of the same material, effectively smoothing the surface, similar to bulk systems,[49] provided that the threshold value for producing defects in the material is not exceeded.

COMPUTATIONAL DETAILS

To get insights into the interaction of the energetic clusters of noble gas atoms with MoS_2 sheets, we performed analytical potential molecular dynamics (MD) simulations using the LAMMPS computational package[50] as detailed below.

Simulation Setup. The simulation setups for the cluster ion irradiation of freestanding and supported MoS_2 monolayers are shown in Figure 1a,b, respectively. The atomic

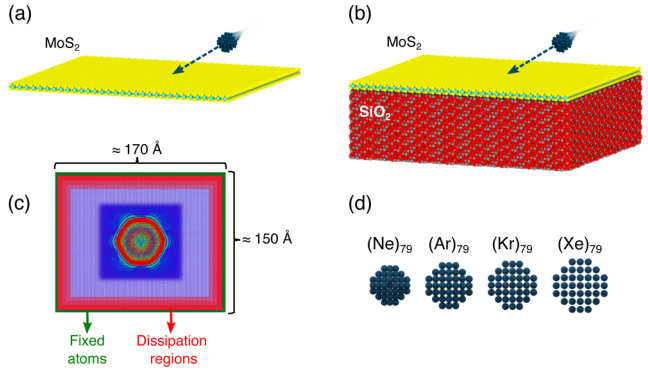

Figure 1. Simulation setup for freestanding (a) and supported (b) MoS_2 monolayers. (c) Top view of the system. The outermost atoms (green) were kept fixed during the irradiation simulations. The kinetic energies of the atoms were scaled in the areas indicated by red. The color scheme of the atoms in the central area illustrates the propagation of a temperature wave after the impact of a cluster. (d) Examples of various noble gas clusters used in our simulations. Heavier clusters have bigger diameters due to larger atom sizes.

geometry of the monolayers was initially optimized using the analytical potentials described below. The target systems were then irradiated with noble gas clusters. The initial (absolute) temperature of the system was zero, and periodic boundary conditions were employed.

The outermost atomic layers were kept fixed during irradiation simulations, as schematically shown in Figure 1c, so that the entire system was not displaced under cluster impacts. To avoid the spurious reflection of heat and pressure waves from the borders of the system, the velocities of the atoms were scaled down in the border areas using the Berendsen thermostat, thus mimicking the energy dissipation in an infinitely large sheet. In fact, three thermostat regions near the supercell boundaries were defined, each with different dissipating powers to precisely dissipate the outgoing energy waves. Free MD was carried out in the central region.

Incident noble gas atom clusters M_N, where M is Ne, Ar, Kr, and Xe and N is the number of atoms, were constructed using the Wulff method, where each cluster has three main facets ({100}, {110}, and {111}). As the orientation of these nonspherical clusters may affect the damage production, in the MD simulations we used three different orientations of the clusters and averaged over them. In the size-dependent simulations, cluster radii varied from 10 to 50 Å, and correspondingly the number of atoms from N = 135 to 15 779. When assessing the effects of incident angle and energy of the cluster, we chose N = 79 due to its "regular" geometry and correspondingly higher stability. The N = 79 clusters

https://dx.doi.org/10.1021/acsami.0c09255
ACS Appl. Mater. Interfaces 2020, 12, 37454−37463

composed from different noble gas atoms are shown in Figure 1d.

The incident cluster energies were in the range of 1−1000 eV/atom, and the incident polar angles varied from normal to grazing (i.e., from 0 to ∼80°). As nuclear stopping is much higher (by a factor of 5−10, depending on the projectile[51]) in this energy range than electronic stopping for the atoms involved in the simulations, we fully disregarded the latter. After cluster impact simulations as described above and reaching a dynamical equilibrium in the central area, the system was quenched to 0 K. The charge state of the cluster cannot be accounted for in the analytical potential MD simulations so that the clusters were assumed to be neutral. As cluster energies we considered are rather small (the corresponding cluster velocities are smaller than the Fermi velocity in MoS_2[52]), one can expect that this approximation did not affect the results, as in the experiment, the clusters should also be neutral upon reaching MoS_2 because of the charge exchange that would take place before the impact.

The sizes of the clusters used in our study are much larger than the primitive cell size of MoS_2, implying that the outcome of a collision should not be very sensitive to the choice of the impact point defined as the intersection of the cluster center-of-mass trajectory with the topmost plane of target atoms. Nonetheless, we sampled over the impact points in the irreducible area in the MoS_2 primitive cell[53] and averaged the results. Twelve impacts per cluster-rotations per irreducible-area, i.e., 36 impacts for each set of parameters (energy, angle, atom-type), were modeled.

The substrate in this work was chosen to be a SiO_2 slab, whose thickness was adjusted depending on cluster energy. Due to the small penetration depth of the incident cluster into the target, atomistic simulations of the actual substrate, instead of the previously used potential-region models,[44] were feasible. Energy dissipation was also implemented at the boundaries of the substrate.

The simulation time, including quenching the system after the impacts, were up to 80 ps. Test simulations with longer times gave essentially the same results. An adaptive time-step method for impact simulations has been used as implemented in LAMMPS.

The area of nanopores produced by cluster impacts was evaluated using the same approach as employed previously[39] to determine pore sizes created after impacts of single ions. In practice, the coordinates of all atoms are projected onto an X−Y plane. In each position, a Gaussian function is introduced to define atom density. Using a certain threshold value, we search for the area with a smaller density, which points to the presence of a pore in the system. When we find the pore, we count the number of missing grid points in the pore area and transform these grid points into the pore size.

Interatomic Potentials. Five different elements (noble gas atom plus two target and two substrate atoms) were involved in every simulation, each of which interacts with its own type and also with the other elements. The used interatomic potentials are reactive empirical bond order (REBO) potential,[54] Tersoff,[55] Lennard-Jones (LJ),[56] and the Ziegler−Biersack−Littmark (ZBL)[57] potentials. To describe the interaction of atoms at small separations, the REBO and Tersoff potentials were splined to the ZBL potential at short atomic distances. The interactions between Mo−Mo, S−S, and Mo−S were modeled by the REBO−ZBL potential, and Tersoff−ZBL was employed to describe the Si−Si, O−O, and Si−O interactions. The choice of the potential for MoS_2 was motivated by a very good reproduction (as compared to other potentials available for this material) of defect formation energies obtained using first-principles calculations.[53] The interactions between the cluster elements (Ne, Ar, Kr, and Xe) with themselves as well as Mo−Si, Mo−O, S−Si, and S−O interactions were described by the LJ potential. All of the LJ parameters used in this work[58−65] are listed in Table 1. The LJ potentials were not splined to the ZBL potentials, as for the atom pairs and the energy range (10−1000 eV/atom) considered in our work, the LJ potential, which behaves as $1/R^{12}$ at small separations, is more repulsive than the ZBL potential. Thus, splining ZBL to the LJ potential is technically more difficult and sometimes not even possible, as splining can either affect the lowest energy configuration or give rise to unphysical "humps" on the energy vs distance curves. Moreover, the analysis of interatomic distances during the impacts for the atom pairs described by the LJ potential indicated that for atoms in the energy range below 50 eV the difference between LJ and ZBL is rather small. Note also that we are primarily interested in the development of damage in the MoS_2 target, while the interactions described by the LJ potentials are not between Mo and S but other atoms, e.g., noble gas atoms or atoms sputtered from the target and substrate atoms. The interactions of the elements constituting the clusters (Ne, Ar, Kr, and Xe) with Mo, S, Si, and O atoms were assumed to be purely repulsive and therefore were treated with the ZBL potential.

Table 1. Parameters of the Lennard-Jones (LJ) Potentials Used in This Work[a]

interaction type	ϵ	σ
Mo−Si	0.00652	3.274
Mo−O	0.00251	2.920
S−Si	0.01439	3.721
S−O	0.00558	3.385
Ne−Ne	0.002947	2.865
Ar−Ar	0.0103	3.45
Kr−Kr	0.014391	3.670
Xe−Xe	0.019156	4.10

[a]The LJ cutoffs are 2.5 times σ.

RESULTS AND DISCUSSION

Figures 2 and 3 present snapshots of the atomic structure from the MD simulations of a cluster impact onto a freestanding and supported MoS_2 sheet, respectively. The front sides of the structures were made partly transparent to make the atomic structure at the impact point visible. It is evident that the response of the systems is quite different, e.g., a high forward sputtering for the freestanding material is observable, while the substrate "stops" the atoms and also gives rise to the development of a larger pressure wave due to the backscattered atoms. Taking this into account, we studied the response of suspended and supported MoS_2 sheets separately and then compared the results.

Freestanding MoS_2 Sheets. One can expect that controllable pore creation in MoS_2 under cluster ion irradiation can be achieved via tuning the following four parameters: element type, cluster size, incident energy, and incident angle. To assess the role of each parameter, we varied one of them while keeping the others fixed.

https://dx.doi.org/10.1021/acsami.0c09255
ACS Appl. Mater. Interfaces 2020, 12, 37454−37463

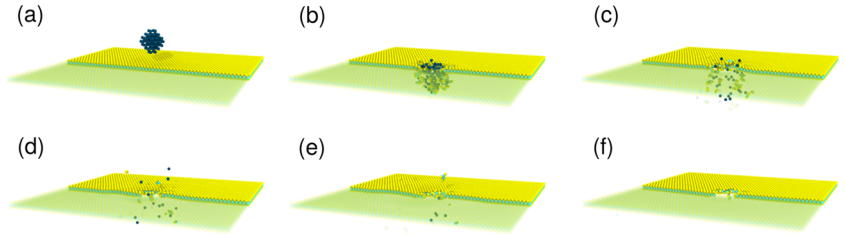

Figure 2. Snapshots from MD simulations of a freestanding MoS_2 monolayer under the impact of a Xe_{79} cluster. The front part of the structures is made partly transparent so that the atomic configurations at the impact point can be seen.

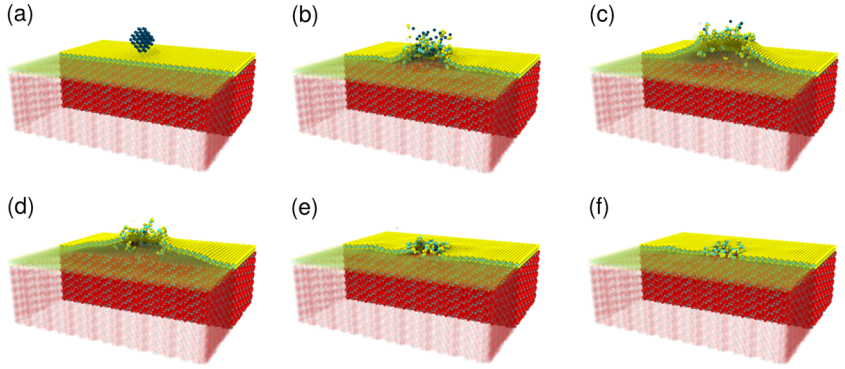

Figure 3. Snapshots from MD simulations of a MoS_2 monolayer on a SiO_2 substrate under the impact of a Xe_{79} cluster. The front part of the structures is made partly transparent so that the atomic configurations at the impact point can be seen.

Response of MoS_2 to Cluster Irradiation: The Dependence on Cluster Energy. We considered first the normal incidence of the clusters. Having carried out the MD simulations as described above, we analyzed the final atomic configuration and calculated the sputtering yield as a function of the incident energy of the cluster. The examples of the atomic structures are presented in Figure 4. Each structure is presented in the final

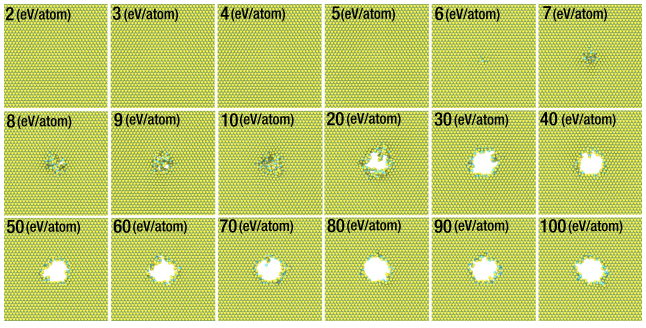

Figure 4. Freestanding MoS_2 sheets after impacts of the Xe_{79} cluster with different initial kinetic energies under normal incidence.

configuration after quenching the kinetic energy of the atoms to zero. It is evident that there is an energy threshold for sputtering, as only above a certain cluster energy holes are formed. Similar results were obtained for other noble gases.

The sputtering yield was defined as the total number of atoms sputtered from the system after a single impact. We also evaluated separately the number of S atoms sputtered from the top (S_{top}) and bottom (S_{bottom}) layers and also the number of Mo atoms. The results are presented in Figure 5 for various noble gases. The energy threshold for sputtering yield is ~5 eV/atom for Ne and is slightly higher ~6 to 7 eV/atom for heavier noble gas atoms. The damage production increases first

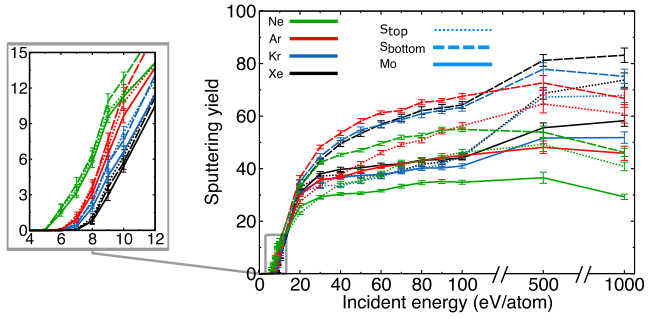

Figure 5. Sputtering yield from a freestanding MoS_2 sheet under the normal incidence of clusters with 79 atoms. Lighter clusters cause more damage at low energies, while it is the other way round at higher energies. The standard error bars are shown.

quickly with cluster energy and then the growth becomes much slower when holes are formed.

While heavier elements sputter more atoms at energies above ~20 eV/atom, the lighter ones (Ne) sputter more atoms at lower energies. This behavior becomes clear when one looks at the sizes of the clusters of different types when containing the same number of atoms (Figure 1d). The heavier clusters have larger diameters due to the larger sizes of the atoms and correspondingly longer interatomic distances. Therefore, the energy transfer per target area for the lighter elements, due to their smaller sizes, is higher and the clusters create more damage at low energies. At low/moderate energies, the higher sputtering yield of S_{bottom} atoms under Ar cluster irradiation is due to the fact that the masses of Ar and S are comparable, which leads to the maximum energy transfer in comparison to other cluster elements, as evident from the head-on binary collision energy transfer formula: $E_{trans} = E_p \times 4m_p m_t/(m_p + m_t)^2$, where E_{trans} is the maximum transferred energy in a binary collision, m_p and m_t are the masses of the projectile and

https://dx.doi.org/10.1021/acsami.0c09255
ACS Appl. Mater. Interfaces 2020, 12, 37454−37463

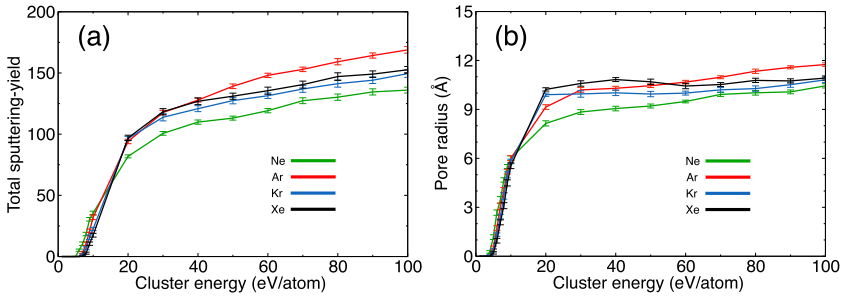

Figure 6. Total sputtering yield from a freestanding MoS_2 sheet (a) as well as the induced pore radius (b) under normal impacts of clusters having 79 noble gas atoms of different types.

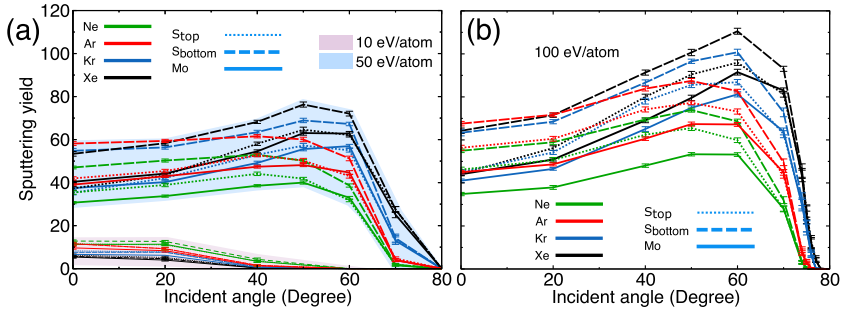

Figure 7. Sputtering yields as a function of the incident angle. (a) Cluster energies are 10 and 50 eV/atom, and the corresponding curves are plotted with different background colors. (b) Cluster energy is 100 eV/atom.

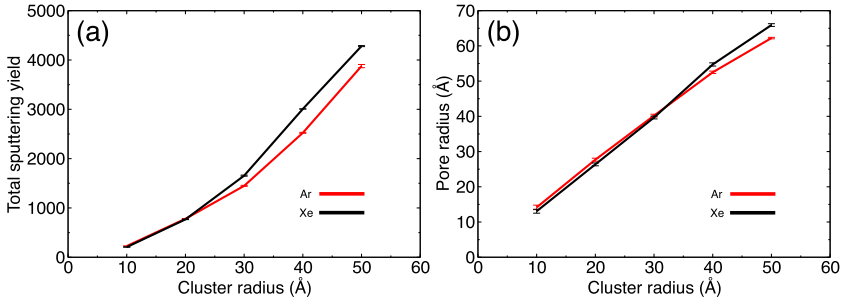

Figure 8. Sputtering yield (a) and pore radius (b) as functions of cluster radius for freestanding MoS_2 under normal impacts of Xe and Ar clusters. The incident energy is 100 eV/atom.

target atoms, respectively, and E_p is the projectile kinetic energy. We stress that the development of damage under cluster impacts is a complicated process, so that the above simple arguments, which help to understand the main trends, should be considered with caution. At high energies, the defect production is governed by the cluster size, and not the energy transfer, followed by its redistribution in the system, as target atoms in the impact area get enough momentum to immediately leave the system and the additional transferred energy is carried away by the sputtered atoms.

The total sputtering yield and the radii of the created pores are shown in Figure 6a,b, respectively, as functions of the incident ion energy. To compensate for the irregular shape of the pores, the diameter of the pores is calculated from the pore area, assuming roughly circular pores (see Figure 4 for the examples). The pore radius−incident energy curve demonstrates a qualitatively similar behavior as the sputter yield−energy relation. There are small differences at intermediate energies, though, when the sputtered atoms with low kinetic energies are unable to leave the system and eventually are reattached to the target elsewhere. Likewise, at low energies and under impacts of lighter clusters, there might be sputtered atoms from only one layer of S atoms, but no pore is created.

Dependence of Defect Production on Angle of Incidence. We also studied the effects of the incident angle of the cluster on defect production. Zero value of the angle corresponds to normal incidence. We chose three different values of cluster incident energies (10, 50, and 100 eV/atom) and calculated sputtering yields as a function of incident angle for different noble gases. The results of the calculations are shown in Figure 7. For 10 eV/atom, no atom is sputtered at angles above ∼60°, while the clusters with higher energies sputter target atoms up to ∼80°. The lighter clusters (Ne and Ar) cause more damage at small incident angles at low and intermediate cluster energies, which originates from their smaller sizes, as discussed in the Response of MoS_2 to Cluster Irradiation: The Dependence on Cluster Energy section. However, at higher energies, the sputtering yield under the impacts of lighter clusters decays faster with angle. For the freestanding system, more S atoms are always sputtered from the bottom layer, as atoms in the upper MoS_2 layers get pushed and transfer their gained momentum to the atoms in the bottom layers.

https://dx.doi.org/10.1021/acsami.0c09255
ACS Appl. Mater. Interfaces 2020, 12, 37454−37463

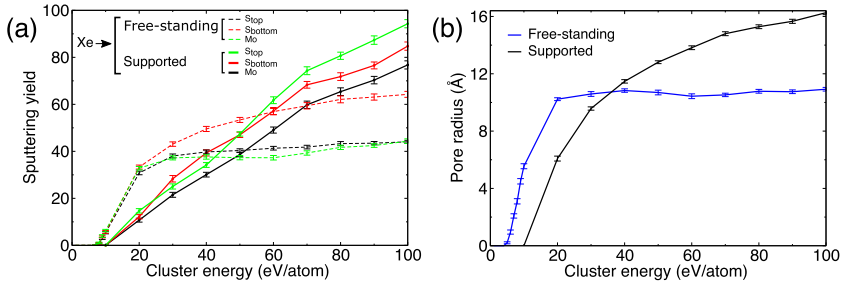

Figure 9. (a) Sputtering yield from a supported MoS_2 sheet under impacts of Xe_{79} clusters with a normal incidence as a function of cluster energy. (b) Radius of the pore created by the impact as a function of cluster energy. The corresponding data for the freestanding system are also given for the sake of comparison.

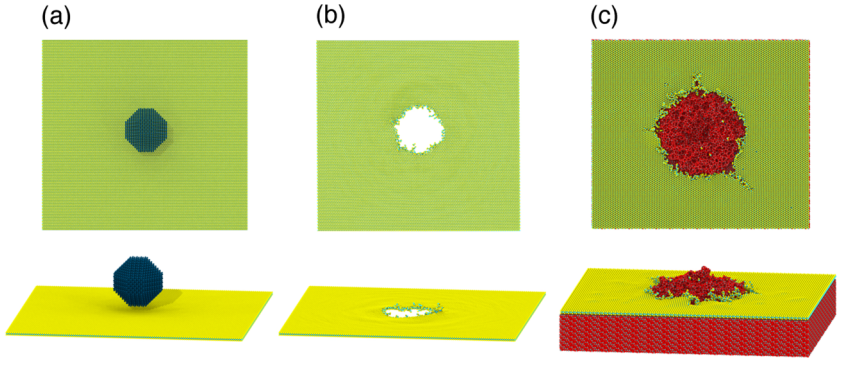

Figure 10. Comparison between impacts of a Xe cluster with a radius of 30 Å and energy 100 eV/atom onto freestanding and supported MoS_2 sheets. Top views (upper panel) and perspective views (lower panel) are presented. The incident angle is normal. (a) System before the impact, (b) pore produced in freestanding MoS_2, and (c) pore produced in supported MoS_2.

Although the dependence of the sputtering yield on cluster energy is weak around 100 eV/atom for normal incidence, this dependence remains strong for large angles (e.g., at ∼60°; Figure 7). This behavior can be understood in terms of the extended impact area of the cluster at high angles, given that the incident energy is high enough to cause damage. In other words, contrary to the normal incidence where the sputtered or noble gas atoms leave the target while they still have substantial energy, the particle at a larger angle has more atoms ahead to transfer its energy to, and hence to cause more damage.

At even larger angles corresponding to grazing trajectories, the cluster atoms interact with a larger number of target atoms, as presumed in the channeling models,[66] instead of the atoms in the cluster-size impact area. Further increase in the incident angle results in a situation where the cluster "sees" the infinite plane of atoms so that sputtering is not possible.

Effects of Cluster Size. To assess the role of the cluster size, we carried out simulations for Ar and Xe clusters, representing medium-mass and high-mass elements. The incident angle was normal, and the cluster energy was chosen to be 100 eV/atom, the regime in which the number of sputtered atoms depends rather weakly on cluster energy, Figure 5. Sputtering yield and radius of the induced pores are plotted against the corresponding cluster radius in Figure 8, panels a and b, respectively. Pore radius depends nearly linearly on the cluster radius, implying that by simply tuning the cluster size, it should be possible to control the size of the pore. We stress that the standard deviation of the pore radius is very small, less than 5%, which indicates that the creation of pores with uniform diameters can be achieved in the experiment.

Note that although the majority of the sputtered atoms in the freestanding case are displaced downward, S atoms in the top layer are occasionally sputtered upward. This behavior may initially seem counterintuitive, but the S_{top} atoms are in fact supported by the heavy Mo layer, so that S atoms may be reflected by Mo atoms. There are even rare cases where the Mo atoms are also among the atoms sputtered upward. These upward-moving Mo atoms however are never found as isolated atoms but always accompanied by S atoms.

Supported MoS_2 Sheets. Having analyzed the response of freestanding MoS_2 to cluster irradiation, we moved on to the supported sheets. We carried out simulations similar to the freestanding case but limited noble atom types to Xe due to a much higher computational cost of these simulations.

Response of Supported MoS_2 to Cluster Irradiation: The Role of Cluster Energy. Sputtering yield upon impacts of Xe_{79} clusters from a supported MoS_2 sheet is presented in Figure 9a as a function of cluster energy. The results for the freestanding material are also given. A comparison of the responses of freestanding and supported MoS_2 layers to cluster irradiation indicates a clear influence of the substrate on damage production. The difference is substantial at both low and high energies as previously reported for single ions.[44] At low energies, the downward sputtering of target atoms is partly suppressed by the substrate. In the high-energy case, where the freestanding MoS_2 membrane stays almost still after the collision, at low cluster energies the MoS_2 membrane swings up and down. However, when supported, the substrate does not allow it to swing. The substrate not only prevents sputtering from the bottom but also takes some of the incident shock energy and dissipates it.

https://dx.doi.org/10.1021/acsami.0c09255
ACS Appl. Mater. Interfaces 2020, 12, 37454−37463

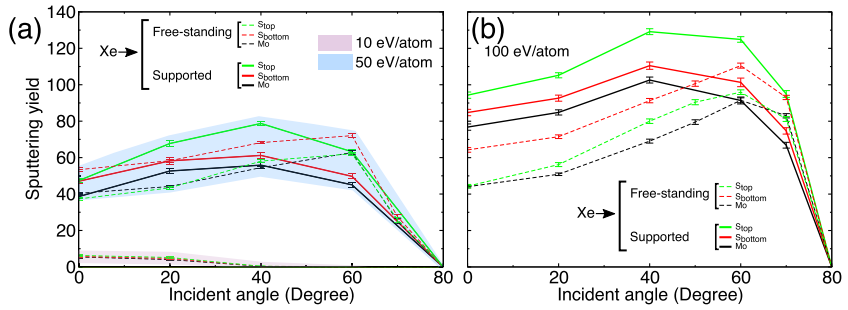

Figure 11. (a) Sputtering yield from a supported MoS_2 sheet under impacts of Xe_{79} clusters as a function of cluster incident angle for cluster energies of 10 and 50 eV/atom. The corresponding data for the freestanding system are also given for the sake of comparison. (b) Results for 100 eV/atom.

The sputtering of bottom S atoms from the freestanding MoS_2 is always dominant, but in the supported sheets, a part of their kinetic energy may be transferred to the top atoms due to the reflection of recoils by the substrate atoms, enhancing the S_{up} sputtering. At high energies, sputtering yield is higher in the supported system. The analysis of atom trajectories indicates that the sheet is damaged by the reflected atoms and atoms sputtered from the substrate, giving rise to the formation of larger holes, as is evident from Figure 9b. One can expect, though, that at high energies exceeding those studied in our work, the pore size should also weakly depend on cluster energy, as the energy will mostly be deposited in the substrate. The standard deviation of the pore radius is also very small, similar to the freestanding system, which indicates that creation of pores with uniform diameters can be experimentally achieved also for supported MoS_2.

The number of sputtered atoms and correspondingly the diameter of the created pores can be noticeably larger than the cluster size, especially for large clusters and at high cluster energies. A snapshot of the impact of a Xe cluster with a diameter of 30 Å onto the supported system is shown in Figure 10c, along with the initial and final atomic configurations for the freestanding system (Figure 10a,b). The size of the pore in the freestanding case is comparable with the cluster size, while for the supported system it (Figure 10c) is considerably larger.

We were unable to systematically study the dependence of pore sizes on cluster diameters as the computational cost of MD simulations increases with the number of atoms, so that collecting statistics for the collisions of big clusters with the supported 2D MoS_2 is computationally very demanding (note that not only the MoS_2 sheet but also the substrate must be large). However, one can expect that the trend is the same as for the freestanding system: the pore size is proportional to the cluster diameter (but is noticeably larger).

Supported MoS_2 under Cluster Impacts: The Effects of Incident Angle. The effects of cluster incident angle on defect and pore creation in supported MoS_2 were investigated with the cluster energies being fixed to 10, 50, and 100 eV/atom. The results of the simulations are presented in Figure 11. It is evident that the presence of a substrate gives rise to the suppression of sputtering at low (10 eV/atom) cluster energy, essentially creating no damage. In the intermediate regime (50 eV/atom), more atoms are sputtered from the top of the MoS_2 sheet for the same cluster energy and angle of incidence than for the freestanding case and the other way around for the bottom layer. The reason for this is discussed in the previous Response of Supported MoS_2 to Cluster Irradiation: The Role of Cluster Energy section: the substrate stops the atoms sputtered from the bottom layer and increases sputtering from the top due to backscattered and recoil atoms. The behavior of the system at high cluster energies (100 eV/atom) is the same as in the intermediate regime. The effect of the substrate is very weak at grazing trajectories when the perpendicular momentum component is very small so that the substrate is not involved, and the overall trend is similar to the freestanding case.

CONCLUSIONS

Using analytical potential MD simulations, we studied the response of MoS_2 sheets, both freestanding and supported by a SiO_2 substrate, to noble gas cluster irradiation. Impacts of clusters with both normal and grazing trajectories composed from various noble gas atoms (Ne, Ar, Kr, and Xe) in a wide range of energies were considered. Our results indicate that when cluster energy is above 20 eV/atom, cluster irradiation can be used to produce pores in 2D MoS_2 sheets, with a diameter depending on the cluster size. For supported MoS_2 sheets, the diameter also depends on cluster energy, while it is essentially independent of cluster energy for the freestanding system (above 100 eV/atom). In both cases, the statistical distribution of the pore diameters is much more uniform as compared to pores created by single ions. This is related to a much larger "effective" impact area and correspondingly a weaker dependence of the collision outcome on the impact parameter. We further showed that energetic clusters can also be used to displace sulfur atoms preferentially from the top or the bottom layer of S atoms in supported MoS_2, which, using subsequent deposition of other chemical elements, can be employed to engineer Janus structures, similar to plasma treatment.[48] These structures allow the tuning of the electronic properties of the material. As no damage is created in MoS_2 sheets at angles exceeding the critical angle (~40° for the supported and ~60° for the freestanding system) and low (~10 eV/atom) energies, cluster irradiation could be used to clean the surface of MoS_2 sheets from adsorbents. Our results for MoS_2, which is the archetypical TMD material, should also be relevant to other members of the TMD family and may suggest new routes toward cluster beam engineering of devices based on 2D inorganic materials and their applications in DNA sequencing, water purification, and molecule separation.

AUTHOR INFORMATION

Corresponding Authors

Sadegh Ghaderzadeh − *Institute of Ion Beam Physics and Materials Research, Helmholtz-Zentrum Dresden-Rossendorf, 01328 Dresden, Germany*; Email: s.ghaderzadeh@hzdr.de

https://dx.doi.org/10.1021/acsami.0c09255
ACS Appl. Mater. Interfaces 2020, 12, 37454−37463

Arkady V. Krasheninnikov − *Institute of Ion Beam Physics and Materials Research, Helmholtz-Zentrum Dresden-Rossendorf, 01328 Dresden, Germany; Department of Applied Physics, Aalto University, 00076 Espoo, Finland;* orcid.org/0000-0003-0074-7588; Email: a.krasheninnikov@hzdr.de

Authors

Vladimir Ladygin − *Institute of Ion Beam Physics and Materials Research, Helmholtz-Zentrum Dresden-Rossendorf, 01328 Dresden, Germany; Moscow Institute of Physics and Technology, Dolgoprudny, Moscow Region 141700, Russia*

Mahdi Ghorbani-Asl − *Institute of Ion Beam Physics and Materials Research, Helmholtz-Zentrum Dresden-Rossendorf, 01328 Dresden, Germany;* orcid.org/0000-0003-3060-4369

Gregor Hlawacek − *Institute of Ion Beam Physics and Materials Research, Helmholtz-Zentrum Dresden-Rossendorf, 01328 Dresden, Germany;* orcid.org/0000-0001-7192-716X

Marika Schleberger − *Fakultät für Physik and CENIDE, Universität Duisburg-Essen, D-47057 Duisburg, Germany;* orcid.org/0000-0002-5785-1186

Complete contact information is available at: https://pubs.acs.org/10.1021/acsami.0c09255

Notes

The authors declare no competing financial interest.

■ ACKNOWLEDGMENTS

The atomic visualizations are created using the Open Visualization Tool (OVITO).[67] The computational support from the Technical University of Dresden computing cluster (TAURUS) and from High-Performance Computing Center (HLRS) in Stuttgart, Germany, directly and also through PRACE project 2018184458 are gratefully appreciated. The structures are generated using the methods implemented in VirtualNanoLab (VNL).[68] This work is part of the npSCOPE project and has received funding from the European Union's Horizon 2020 research and innovation program (grant no. 720964). We also thank the DFG for support within the projects SCHL 384/20-1 (project no. 406129719) and KR 4866/2-1 (project no. 406129719).

■ REFERENCES

(1) Novoselov, K. S.; Jiang, D.; Schedin, F.; Booth, T. J.; Khotkevich, V.; Morozov, S.; Geim, A. K. Two-dimensional Atomic Crystals. *Proc. Natl. Acad. Sci. U.S.A.* **2005**, *102*, 10451−10453.

(2) Ferrari, A. C.; et al. Science and Technology Roadmap for Graphene, Related Two-Dimensional Crystals, and Hybrid Systems. *Nanoscale* **2015**, *7*, 4598−4810.

(3) Wang, L.; Boutilier, M. S.; Kidambi, P. R.; Jang, D.; Hadjiconstantinou, N. G.; Karnik, R. Fundamental Transport Mechanisms, Fabrication and Potential Applications of Nanoporous Atomically Thin Membranes. *Nat. Nanotechnol.* **2017**, *12*, 509−522.

(4) Danda, G.; Drndić, M. Two-Dimensional Nanopores and Nanoporous Membranes for Ion and Molecule Transport. *Curr. Opin. Biotechnol.* **2019**, *55*, 124−133.

(5) Wanunu, M. Nanopores: A Journey Towards DNA Sequencing. *Phys. Life Rev.* **2012**, *9*, 125−158.

(6) Garaj, S.; Hubbard, W.; Reina, A.; Kong, J.; Branton, D.; Golovchenko, J. Graphene as a Subnanometre Trans-Electrode Membrane. *Nature* **2010**, *467*, 190−193.

(7) Venkatesan, B. M.; Bashir, R. Nanopore Sensors for Nucleic Acid Analysis. *Nat. Nanotechnol.* **2011**, *6*, 615−624.

(8) Clarke, J.; Wu, H.-C.; Jayasinghe, L.; Patel, A.; Reid, S.; Bayley, H. Continuous Base Identification for Single-Molecule Nanopore DNA Sequencing. *Nat. Nanotechnol.* **2009**, *4*, 265−270.

(9) Bai, J.; Zhong, X.; Jiang, S.; Huang, Y.; Duan, X. Graphene Nanomesh. *Nat. Nanotechnol.* **2010**, *5*, 190−194.

(10) Jessen, B. S.; Gammelgaard, L.; Thomsen, M. R.; Mackenzie, D. M. A.; Thomsen, J. D.; Caridad, J. M.; Duegaard, E.; Watanabe, K.; Taniguchi, T.; Booth, T. J.; Pedersen, T. G.; Jauho, A.-P.; Bøggild, P. Lithographic Band Structure Engineering of Graphene. *Nat. Nanotechnol.* **2019**, *14*, 340−346.

(11) Lin, Y.; Watson, K. A.; Kim, J.-W.; Baggett, D. W.; Working, D. C.; Connell, J. W. Bulk Preparation of Holey Graphene via Controlled Catalytic Oxidation. *Nanoscale* **2013**, *5*, 7814−7824.

(12) Zhao, X.; Kotakoski, J.; Meyer, J. C.; Sutter, E.; Sutter, P.; Krasheninnikov, A. V.; Kaiser, U.; Zhou, W. Engineering and Modifying Two-Dimensional Materials by Electron Beams. *MRS Bull.* **2017**, *42*, 667−676.

(13) Krasheninnikov, A. V.; Banhart, F. Engineering of Nanostructured Carbon Materials with Electron or Ion Beams. *Nat. Mater.* **2007**, *6*, 723−733.

(14) Schleberger, M.; Kotakoski, J. 2D Material Science: Defect Engineering by Particle Irradiation. *Materials* **2018**, *11*, No. 1885.

(15) He, K.; Robertson, A. W.; Gong, C.; Allen, C. S.; Xu, Q.; Zandbergen, H.; Grossman, J. C.; Kirkland, A. I.; Warner, J. H. Controlled Formation of Closed-Edge Nanopores in Graphene. *Nanoscale* **2015**, *7*, 11602−11610.

(16) Fischbein, M. D.; Drndić, M. Electron Beam Nanosculpting of Suspended Graphene Sheets. *Appl. Phys. Lett.* **2008**, *93*, No. 113107.

(17) Song, B.; Schneider, G. F.; Xu, Q.; Pandraud, G.; Dekker, C.; Zandbergen, H. Atomic-Scale Electron-Beam Sculpting of Near-Defect-Free Graphene Nanostructures. *Nano Lett.* **2011**, *11*, 2247−2250.

(18) Kotakoski, J.; Krasheninnikov, A. V.; Kaiser, U.; Meyer, J. C. From Point Defects in Graphene to Two-Dimensional Amorphous Carbon. *Phys. Rev. Lett.* **2011**, *106*, No. 105505.

(19) Jin, C.; Lin, F.; Suenaga, K.; Iijima, S. Fabrication of a Freestanding Boron Nitride Single Layer and Its Defect Assignments. *Phys. Rev. Lett.* **2009**, *102*, No. 195505.

(20) Meyer, J. C.; Chuvilin, A.; Algara-Siller, G.; Biskupek, J.; Kaiser, U. Selective Sputtering and Atomic Resolution Imaging of Atomically Thin Boron Nitride Membranes. *Nano Lett.* **2009**, *9*, 2683−2689.

(21) Fan, Y.; Robertson, A. W.; Zhou, Y.; Chen, Q.; Zhang, X.; Browning, N. D.; Zheng, H.; Rümmeli, M.; Warner, J. H. Electrical Breakdown of Suspended Mono- and Few-Layer Tungsten Disulfide via Sulfur Depletion Identified by in Situ Atomic Imaging. *ACS Nano* **2017**, *11*, 9435−9444.

(22) Lehtinen, O.; Komsa, H. P.; Pulkin, A.; Whitwick, M. B.; Chen, M. W.; Lehnert, T.; Mohn, M. J.; Yazyev, O. V.; Kis, A.; Kaiser, U.; Krasheninnikov, A. V. Atomic Scale Microstructure and Properties of Se-Deficient Two-Dimensional $MoSe_2$. *ACS Nano* **2015**, *9*, 3274−3283.

(23) Zhou, W.; Zou, X.; Najmaei, S.; Liu, Z.; Shi, Y.; Kong, J.; Lou, J.; Ajayan, P. M.; Yakobson, B. I.; Idrobo, J.-C. Intrinsic Structural Defects in Monolayer Molybdenum Disulfide. *Nano Lett.* **2013**, *13*, 2615−2622.

(24) Thiruraman, J. P.; Masih Das, P.; Drndić, M. Irradiation of Transition Metal Dichalcogenides Using a Focused Ion Beam: Controlled Single-Atom Defect Creation. *Adv. Funct. Mater.* **2019**, *29*, No. 1904668.

(25) He, Z.; Zhao, R.; Chen, X.; Chen, H.; Zhu, Y.; Su, H.; Huang, S.; Xue, J.; Dai, J.; Cheng, S.; Liu, M.; Wang, X.; Chen, Y. Defect Engineering in Single-Layer MoS_2 Using Heavy Ion Irradiation. *ACS Appl. Mater. Interfaces* **2018**, *10*, 42524−42533.

(26) Thiruraman, J. P.; Fujisawa, K.; Danda, G.; Das, P. M.; Zhang, T.; Bolotsky, A.; Perea-López, N.; Nicolaï, A.; Senet, P.; Terrones, M.; Drndić, M. Angstrom-Size Defect Creation and Ionic Transport through Pores in Single-Layer MoS_2. *Nano Lett.* **2018**, *18*, 1651−1659.

(27) Bangert, U.; Pierce, W.; Kepaptsoglou, D. M.; Ramasse, Q.; Zan, R.; Gass, M. H.; Van den Berg, J. A.; Boothroyd, C. B.; Amani, J.; Hofsäss, H. Ion Implantation of Graphene-Toward IC Compatible Technologies. *Nano Lett.* **2013**, *13*, 4902−4907.
(28) Tripathi, M.; Markevich, A.; Böttger, R.; Facsko, S.; Besley, E.; Kotakoski, J.; Susi, T. Implanting Germanium Into Graphene. *ACS Nano* **2018**, *12*, 4641−4647.
(29) Bell, D. C.; Lemme, M. C.; Stern, L. A.; Williams, J. R.; Marcus, C. M. Precision Cutting and Patterning of Graphene with Helium Ions. *Nanotechnology* **2009**, *20*, No. 455301.
(30) Fox, D.; Zhou, Y. B.; O'Neill, A.; Kumar, S.; Wang, J. J.; Coleman, J. N.; Duesberg, G. S.; Donegan, J. F.; Zhang, H. Z. Helium Ion Microscopy of Graphene: Beam Damage, Image Quality and Edge Contrast. *Nanotechnology* **2013**, *24*, No. 335702.
(31) Fox, D. S.; et al. Nanopatterning and Electrical Tuning of MoS_2 Layers with a Subnanometer Helium Ion Beam. *Nano Lett.* **2015**, *15*, 5307−5313.
(32) Schmidt, M. E.; Iwasaki, T.; Muruganathan, M.; Haque, M.; Ngoc, H. V.; Ogawa, S.; Mizuta, H. Structurally Controlled Large-Area 10 nm Pitch Graphene Nanomesh by Focused Helium Ion Beam Milling. *ACS Appl. Mater. Interfaces* **2018**, *10*, 10362−10368.
(33) Yoon, K.; Rahnamoun, A.; Swett, J. L.; Iberi, V.; Cullen, D. A.; Vlassiouk, I. V.; Belianinov, A.; Jesse, S.; Sang, X.; Ovchinnikova, O. S.; Rondinone, A. J.; Unocic, R. R.; Van Duin, A. C. Atomistic-Scale Simulations of Defect Formation in Graphene under Noble Gas Ion Irradiation. *ACS Nano* **2016**, *10*, 8376−8384.
(34) Maguire, P.; Fox, D. S.; Zhou, Y.; Wang, Q.; O'Brien, M.; Jadwiszczak, J.; Cullen, C. P.; McManus, J.; Bateman, S.; McEvoy, N.; Duesberg, G. S.; Zhang, H. Defect Sizing, Separation, and Substrate Effects in Ion-Irradiated Monolayer Two-Dimensional Materials. *Phys. Rev. B* **2018**, *98*, No. 134109.
(35) Madauß, L.; Ochedowski, O.; Lebius, H.; Ban-d'Etat, B.; Naylor, C. H.; Johnson, A. T. C.; Kotakoski, J.; Schleberger, M. Defect Engineering of Single- and Few-Layer MoS_2 by Swift Heavy Ion Irradiation. *2D Mater.* **2016**, *4*, No. 015034.
(36) Clochard, M. C.; Melilli, G.; Rizza, G.; Madon, B.; Alves, M.; Wegrowe, J. E.; Toimil-Molares, M. E.; Christian, M.; Ortolani, L.; Rizzoli, R.; Morandi, V.; Palermo, V.; Bianco, S.; Pirri, F.; Sangermano, M. Large Area Fabrication of Self-Standing Nanoporous Graphene-on-PMMA Substrate. *Mater. Lett.* **2016**, *184*, 47−51.
(37) Vázquez, H.; Åhlgren, E.; Ochedowski, O.; Leino, A.; Mirzayev, R.; Kozubek, R.; Lebius, H.; Karlušic, M.; Jakšic, M.; Krasheninnikov, A.; Kotakoski, J.; Schleberger, M.; Nordlund, K.; Djurabekova, F. Creating Nanoporous Graphene With Swift Heavy Ions. *Carbon* **2017**, *114*, 511−518.
(38) Gruber, E.; et al. Ultrafast Electronic Response of Graphene to a Strong and Localized Electric Field. *Nat. Commun.* **2016**, *7*, No. 13948.
(39) Kozubek, R.; Tripathi, M.; Ghorbani-Asl, M.; Kretschmer, S.; Madauß, L.; Pollmann, E.; O'Brien, M.; McEvoy, N.; Ludacka, U.; Susi, T.; et al. Perforating Freestanding Molybdenum Disulfide Monolayers with Highly Charged Ions. *J. Phys. Chem. Lett.* **2019**, *10*, 904−910.
(40) Zhao, S.; Xue, J.; Liang, L.; Wang, Y.; Yan, S. Drilling Nanopores in Graphene with Clusters: A Molecular Dynamics Study. *J. Phys. Chem. C* **2012**, *116*, 11776−11782.
(41) Inui, N.; Mochiji, K.; Moritani, K.; Nakashima, N. Molecular Dynamics Simulations of Nanopore Processing in a Graphene Sheet by using Gas Cluster Ion Beam. *Appl. Phys. A* **2010**, *98*, 787−794.
(42) Zabihi, Z.; Araghi, H. Formation of Nanopore in a Suspended Graphene Sheet with Argon Cluster Bombardment: a Molecular Dynamics Simulation Study. *Nucl. Instrum. Methods Phys. Res., Sect. B* **2015**, *343*, 48−51.
(43) Abadi, R.; Shirazi, A. H. N.; Izadifar, M.; Sepahi, M.; Rabczuk, T. Fabrication of Nanopores in Polycrystalline Boron-Nitride Nanosheet by using Si, SiC and Diamond Clusters Bombardment. *Comput. Mater. Sci.* **2018**, *145*, 280−290.
(44) Kretschmer, S.; Maslov, M.; Ghaderzadeh, S.; Ghorbani-Asl, M.; Hlawacek, G.; Krasheninnikov, A. V. Supported Two-Dimensional Materials under Ion Irradiation: The Substrate Governs Defect Production. *ACS Appl. Mater. Interfaces* **2018**, *10*, 30827−30836.
(45) Kalbac, M.; Lehtinen, O.; Krasheninnikov, A. V.; Keinonen, J. Ion-Irradiation-Induced Defects in Isotopically-Labeled Two Layered Graphene: Enhanced In-Situ Annealing of the Damage. *Adv. Mater.* **2013**, *25*, 1004−1009.
(46) Yin, K.; Huang, S.; Chen, X.; Wang, X.; Kong, J.; Chen, Y.; Xue, J. Generating Sub-Nanometer Pores in Single-Layer MoS_2 by Heavy-Ion Bombardment for Gas Separation: A Theoretical Perspective. *ACS Appl. Mater. Interfaces* **2018**, *10*, 28909−28917.
(47) Li, W.; Yang, Y.; Weber, J. K.; Zhang, G.; Zhou, R. Tunable, Strain-Controlled Nanoporous MoS_2 Filter for Water Desalination. *ACS Nano* **2016**, *10*, 1829−1835.
(48) Ma, Q.; et al. Controlled Argon Beam-Induced Desulfurization of Monolayer Molybdenum Disulfide. *J. Phys.: Condens. Matter* **2013**, *25*, No. 252201.
(49) Hirota, T.; Toyoda, N.; Yamamoto, A.; Yamada, I. Modification and Smoothing of Patterned Surface by Gas Cluster Ion Beam Irradiation. *Appl. Surf. Sci.* **2009**, *256*, 1110−1113.
(50) Plimpton, S. Fast Parallel Algorithms for Short-Range Molecular Dynamics. *J. Comput. Phys.* **1995**, *117*, 1−19.
(51) Program TRIM by Ziegler, J. F., Biersack, J. P. http://www.srim.org.
(52) Kolobov, A. V.; Tominaga, J. *Two-Dimensional Transition Metal Dichalcogenides*; Springer, 2016.
(53) Ghorbani-Asl, M.; Kretschmer, S.; Spearot, D. E.; Krasheninnikov, A. V. Two-Dimensional MoS_2 under Ion Irradiation: from Controlled Defect Production to Electronic Structure Engineering. *2D Mater.* **2017**, *4*, No. 025078.
(54) Liang, T.; Phillpot, S. R.; Sinnott, S. B. Parametrization of a Reactive Many-Body Potential for Mo−S systems. *Phys. Rev. B* **2009**, *79*, No. 245110.
(55) Tersoff, J. Modeling solid-State Chemistry: Interatomic Potentials for Multicomponent Systems. *Phys. Rev. B* **1989**, *39*, No. 5566.
(56) Lennard-Jones, J. E. Cohesion. *Proc. Phys. Soc.* **1931**, *43*, 461.
(57) Zeigler, J.; Biersack, J.; Littmark, U. The Stopping and Range of Ions in Solids. In *Treatise on Heavy-Ion Science*; Springer: Boston, MA, 1985; pp 93−129.
(58) Yamaguchi, Y.; Gspann, J. Large-Scale Molecular Dynamics Simulations of High Energy Cluster Impact on Diamond Surface. *Eur. Phys. J. D* **2001**, *16*, 103−106.
(59) Dawid, A.; Gburski, Z. Interaction-Induced Light Scattering in Lennard-Jones Argon Clusters: Computer Simulations. *Phys. Rev. A* **1997**, *56*, No. 3294.
(60) Hoheisel, C. Ne/Xe at very High Pressures: A Molecular Dynamics Study using Lennard-Jones (12−6) Potentials. *Mol. Phys.* **1987**, *62*, 385−396.
(61) Vogelsang, R.; Hoheisel, C. Thermal Conductivity of a Binary-Liquid Mixture Studied by Molecular Dynamics with use of Lennard-Jones Potentials. *Phys. Rev. A* **1987**, *35*, No. 3487.
(62) Munro, L. J.; Tharrington, A.; Jordan, K. D. Global Optimization and Finite Temperature Simulations of Atomic Clusters: Use of Xe_nAr_m Clusters as Test Systems. *Comput. Phys. Commun.* **2002**, *145*, 1−23.
(63) Scharf, D.; Jortner, J.; Landman, U. Excited-State Dynamics of Rare-Gas Clusters. *J. Chem. Phys.* **1988**, *88*, 4273−4288.
(64) Rappé, A. K.; Casewit, C. J.; Colwell, K.; Goddard, W. A., III; Skiff, W. M. UFF, a Full Periodic Table Force Field for Molecular Mechanics and Molecular Dynamics Simulations. *J. Am. Chem. Soc.* **1992**, *114*, 10024−10035.
(65) Suryavanshi, S. V.; Gabourie, A. J.; Farimani, A. B.; Yalon, E.; Pop, E. In *Thermal Boundary Conductance of the MOS_2-SiO_2 Interface*, 2017 IEEE 17th International Conference on Nanotechnology (IEEE-NANO), 2017; pp 26−29.
(66) Nordlund, K.; Hobler, G. Dependence of Ion Channeling on Relative Atomic Number in Compounds. *Nucl. Instrum. Methods Phys. Res., Sect. B* **2018**, *435*, 61−69.

https://dx.doi.org/10.1021/acsami.0c09255
ACS Appl. Mater. Interfaces 2020, 12, 37454−37463

(67) Stukowski, A. Visualization and Analysis of Atomistic Simulation Data with OVITO–the Open Visualization Tool. *Modell. Simul. Mater. Sci. Eng.* **2009**, *18*, No. 015012.
(68) Schneider, J.; Hamaekers, J.; Chill, S. T.; Smidstrup, S.; Bulin, J.; Thesen, R.; Blom, A.; Stokbro, K. ATK-ForceField: A New Generation Molecular Dynamics Software Package. *Modell. Simul. Mater. Sci. Eng.* **2017**, *25*, No. 085007.

https://dx.doi.org/10.1021/acsami.0c09255
ACS Appl. Mater. Interfaces 2020, 12, 37454–37463